평면 광도파로 상의 식각 브래그 격자를 이용한 광온도 센서의 개발

안국찬† · 이상매*

진주산업대학교 기계설계공학과 · *미 신시내티대학교 전기공학과 극소전자센서 및 MEMS 센터

(2000. 6. 1. 접수 / 2001. 5. 30. 채택)

Optical Temperature Sensor Based on the Etched Planar Waveguide Bragg Grating Considering Linear Thermo-optic Effect

Kook-Chan Ahn† · Sang-Mae Lee*

Department of Mechanical Design Engineering, Cheju National University · *Department of Microelectronic Sensors and MEMS, Department of Electrical & Computer engineering and Computer Science, University of Cincinnati

(Received June 1, 2000 / Accepted May 30, 2001)

Abstract : This paper demonstrates the development of optical temperature sensor based on the etched planar waveguide Bragg grating. Topics include design and fabrication of the etched planar waveguide Bragg grating, investigation of the grating reflection characteristics, and temperature measurement capabilities. The typical bandwidth and reflectivity of the surface etched grating has been ~0.2 nm and ~7%, respectively, at a wavelength of ~1552 nm. The temperature-induced wavelength change of the optical sensor is found to be slightly non-linear over ~200°C temperature range. Theoretical models for the grating response of the sensor based on waveguide and plate deformation theories agree with experiments to within acceptable tolerance.

초 록 : 본 논문은 식각된 평면 광도파 브래그 격자를 이용한 광온도 센서의 개발에 대한 연구로써 식각된 평면 도파로 브래그 격자의 설계, 제작, 격자 특성 연구 및 온도 측정 가능성을 주 연구 목적으로 하고 있다. 평면 식각 브래그 격자 센서의 전형적 대역폭과 그 반사도는 각각 ~1,522nm의 파장에서 ~0.2nm와 ~7%이며, 200°C까지 온도가 변화하는 동안 온도 변화에 따른 브래그 파장의 변화는 약간의 비선형성을 보였다. 광도파로와 판변형이론에 기초한 브래그 격자의 온도 변화에 따른 광파장 응답을 예측하기 위한 이론적 모델은 실험과 비교할 때 허용 오차내에서 잘 일치하고 있다.

Key Words : optical temperature sensor, etched planar waveguide bragg grating, linear thermo-optic effect

1. INTRODUCTION

High-temperature strain measurements are critical to understanding constitutive properties of new high- temperature materials such as metal matrix composites (MMCs), ceramic matrix composites (CMCs), and carbon/carbon composites (CCCs), as well as for determining the mechanical reliability of components produced from these materials. These materials are finding greater use in applications involving advanced aeropropulsion systems such as the reusable Launch Vehicle or the high speed civil transport. Strain gages most commonly used in high temperature measurements are resistance based foil strain gages[1~4] or capacitance based strain gages[5~7], and are all limited operating temperature of less than ~850°C. The recent entry in high temperature strain sensing field are transducers based on cylindrical optical waveguides (optical fibers) produced from amorphous silica[8,9] and sapphire[10,11]. Silica based optical fiber sensors have been demonstrated up to 1200°C, while sapphire-based sensors have been demonstrated in temperature regimes near 1700°C. While sapphire sensors are attractive for high temperature sensor applications, they face a number of technical challenges. Optical grade sapphire fibers are

†To whom correspondence should be addressed.
kcahn@chinju.ac.kr

difficult and expensive to fabricate, and only available in short segments. Additionally, the sapphire fiber sensors utilized the fiber Fabry-Perot interferometer far developed show limited promise for multiplexing. The silica-based sensors described in Refs. [8] and [9] face similar limitations with regard to multiplexing.

In-fiber Bragg grating sensors, on the other hand, have excellent multiplexing potential and therefore it is worth investigating how Bragg grating structures can be used to develop high temperature strain sensors. The kinetics of Bragg grating growth in photosensitive fiber has shown that the temperature stability of in-fiber Bragg grating is different for Type I and Type II gratings, with Type I and Ia gratings being limited to ~250°C[12,13] and Type II grating being limited to ~800°C[14~16]. The temperature capability of Type II gratings rivals the operational temperature capabilities of traditional resistance and capacitance high temperature strain gages.

This paper describes a preliminary study of Bragg grating sensors etched into planar waveguide structures as a means of increasing the operational temperature range of the gratings, while at the same time preserving the multiplexing capability of Bragg grating sensors. These gratings are created by modifying the waveguide geometry instead of optical properties, and thus it may be possible to use them up to softening point of silica (roughly 1200°C). The fabrication procedures for the proposed Bragg grating sensors can be very controllable, and show promise for cost effective mass production using the same technology employed by the microelectronics industry. These types of grating structures have been used in distributed feedback lasers, grating couplers, modulators, and filters, etc.[17~21]. As a first step towards developing etched planar waveguide Bragg grating strain sensors, this paper develops mathematical model and fabrication techniques necessary for investing the optical and mechanical properties.

2. MATHEMATICAL BACKGROUND

This section provides the basic mathematical foundation that will be used to design and perform data

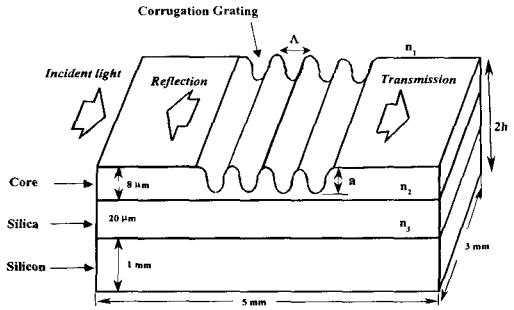

Fig. 1. Schematic diagram of the planar waveguide with surface corrugation grating

analyses of the proposed planar waveguide etched grating sensor. This section starts by providing the expressions needed to calculate the propagation constants for the slab waveguide in terms of the waveguide geometric and optical properties. Then the coupled mode equations used to determine the grating properties are presented. The waveguide geometry of interest in this paper is illustrated in Fig. 1, and consists of a germanium doped SiO_2 core bounded by air above and pure SiO_2 below.

This waveguide is fabricated on a silicon substrate. The refractive index of air, core and cladding SiO_2 layers are denoted by n_1, n_2, and n_3, respectively and core thickness is given by t_g. Also seen in Fig. 1 are the etched corrugations of pitch Λ and depth a.

The most important parameter in the design of Bragg grating in slab waveguides is effective index. This effective index is found in the usual way[22] by solving the wave equation and applying continuity boundary conditions at the respective core/cladding interfaces of the waveguide shown in Fig. 1. The guided modes have propagation constant β_s such that $k_0 n_3 < \beta_s < k_0 n_2$, where $n_1 < n_3$. This solution process leads to the following transcendental equation that yields the propagation constant:

$$\tanh t_g \quad \frac{p+q}{h(1-pq/h^2)} \tag{1}$$

where $h=(n_y^2 k_0^2-\beta_s^2)^{1/2}$, $q=(\beta^2-n_1^2 k_0^2)^{1/2}$ and $p=(\beta_s^2-n_3^2 k_0^2)^{1/2}$ and $k_0 \cong \omega/c = 2\pi/\lambda$.

Given a set of refractive indices n_1, n_2, and n_3 and waveguide thickness, t_g, of the planar waveguide, and

source wavelength, λ. Eq. (1) in general yields a number of solutions for the propagation constant, β_s. However, the source wavelength and waveguide thickness are restricted in the present study such that only one propagation mode is supported, and therefore Eq. (1) has only one solution of interest. As a result, the effective index of the waveguide is given by $n_{eff} = \beta_s \lambda / 2\pi$

The corrugated structure into the waveguide leads to a corresponding periodic perturbation of the refractive index distribution. Each groove of the grating acts like a weak mirror, and the cumulative effect of all of the weak reflectors results in a very strong combined reflection centered on what is known as the Bragg wavelength. The Bragg wavelength[22] is related to the effective index calculated above and grating period, Λ,

$$\lambda_b = 2 n_{eff} \Lambda \tag{2}$$

which when expressed in terms of the propagation constant is given by

$$\lambda_b = \beta_s \lambda \Lambda / 2 \tag{3}$$

where λ_b is the Bragg wavelength and λ is the central wavelength of the optical source. The fraction of power couple to the backward-propagation mode (- β_s), i.e. the grating reflectivity[22] is given by

$$R_{\max} = \tanh^2(\kappa L) \tag{4}$$

where L is the length of the Bragg grating and the coupling coefficient is $\kappa = (\pi h / \lambda_0)(n_2 - n_{eff}) / (2 n_{eff} / w_{eff})$. n_{eff} is the effecitive index of the waveguide core and w_{eff} is the effective thickness of the waveguide guiding layer. Eqs. (1) through (4) are used to perform preliminary design of the planar waveguide grating sensor, and to guide the experimental program.

3. FABRICATION OF SENSOR

The planar waveguides used in these studies are fabricated by Photonics Integrated Research Inc. (PIRI) using hydrolysis deposition[23]. These waveguides are originally manufactured with an 8 μm thick germanium doped silica core with a 20 μm silica undercladding sitting on top of a 1 mm thick silicon substrate. The refractive indices of the core layer and undercladding layer are 1.4495 and 1.4452 measured at 1.55 μm wavelength, respectively. The waveguide blank is diced parallel or perpendicular to the straight edge of the silicon substrate into 3 mm long x 5 mm wide waveguides.

Bragg gratings are produced in the planar waveguides using photoresist based optical lithography techniques. This process starts by first spin coating a 50 % dilution of Shipley S1400-17 photoresist onto the surface of the waveguide using 6000 rev/min for 30 seconds. The resulting ~220 nm layer of photoresist is soft baked for 35 min at 96°C to ensure complete removal of thinning solvents. A phase mask printing method is then used to fabricate Bragg gratings[24,25], as shown in Fig. 2.

A phase mask is used to produce two equal amplitude interfering optical beams. The interfering pattern is expanded in size so that interference occurs in a 2 mm smaller diameter circular region. Grating are typically written in planar waveguide coated by exposing the photoresist to the 244 nm UV light for 5 sec to 8 sec with a laser powers ranging from 2 mW to 3 mW. The phase mask used in this study had a pitch of 0.5278 μm and 15.4 % transmission of zeroith order diffraction. This phase mask pitch corresponds to a Bragg wavelength somewhat near 1550 nm, depending on the effective index of the waveguide. Once exposed, the waveguides are baked for 12 min at 120°C.

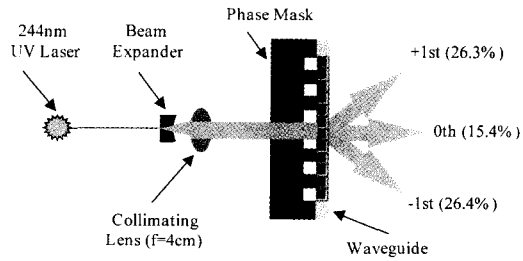

Fig. 2. Schematic configuration of the optical phase mask printing setup for fabrication of Bragg grating

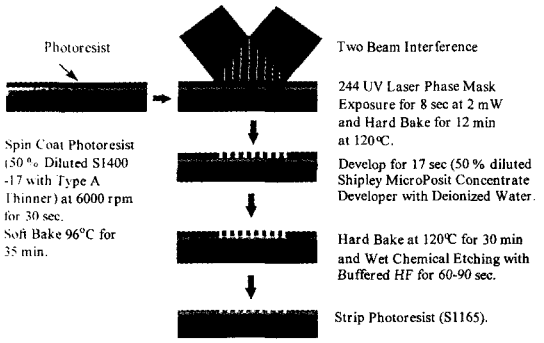

Fig. 3. Lithographic procedures of fabrication of the grating on the waveguide

The next step in the grating fabrication process shown in Fig. 3 involves developing the photoresist for typically 12 sec with a developer made of one part Shipley Microposit Concentrate and one part deionized water to form resist gratings. The waveguide are then rinsed in deionized water for 30 sec and then blown dry with Nitrogen gas. After developing, the substrates are baked for 30 min at 120°C, and then are wet-chemically etched for 75 seconds to a depth of 130 nm to 200 nm using bufferd HF[26]. Next, the photo-resist is stripped using solvents such as Shipley S1165 remover or acetone.

The gratings investigated here typically have a 537.8 nm period as measured using an Atomic Force Microscopy (AFM) shown in Fig. 4. It was very difficult to obtain a homogeneous grating structure because the zeroith order diffracted beam from the phase mask caused unwanted fringe patterns, resulting from multiple reflections between the waveguide and the phase mask. It is noted that the distance between the phase mask and the waveguide has to be minimized without causing the damage of the phase mask to minimize the above noted multiple reflections.

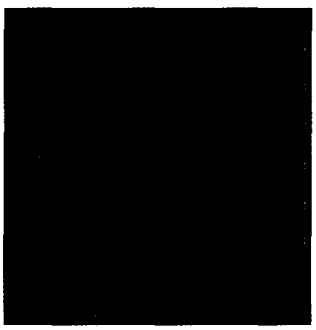

Fig. 4. Photographs of the etched Bragg grating formed on the waveguide using an atomic force microscop

The final step in the grating sensor fabrication process is to prepare the edges of the waveguides to facilitate coupling light into the sensor and to provide for visual inspection. This is done by first cleaning the diced waveguide with solvents (acetone and methanol) and then blow drying it with nitrogen gas. The waveguide is mounted on a jig with the heat-melt wax and is polished using 1 micron and 0.3 micron aluminum oxide on a polishing wheel rotating at 1500 rev/min. The polishing is done using 0.1 micron diamond sheet. Visually inspection using a transmission optical microscope is used to control the surface roughness of the waveguide facet. Finally, the polished waveguide is thoroughly cleaned in acetone for 30 min at 70°C to remove residual wax.

4. BUTT COUPLING TECHNIQUES

The etched grating sensor is interrogated by using a single mode optical fiber to carry the light to and from the sensors. This means that efficient fiber to waveguide coupling techniques must be used. Tolerancing type of lowest insertion losses are offset less than ± 2 μm and an angular misalignment less than 0.5°[27]. The butt coupling technique used to achieve the efficient fiber to waveguide coupling is shown schematically in Fig. 5. Amplified Spontaneous Emission (ASE) from an Erbium Doped Fiber Amplifier (EDFA) is launched into one arm of a 3 dB coupler fabricated with optical fiber having a mode field diameter of 9.5 μm. One arm of the coupler is index matched to prevent back reflection and the other arm is butt coupled into the

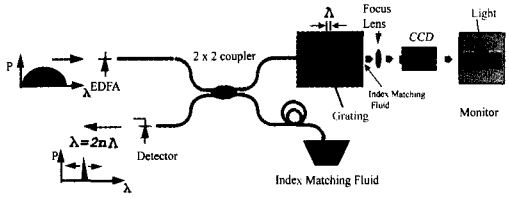

Fig. 5. Schematic configuration of the coupling technique used to investigate spectral characteristics of planar waveguide Bragg gratings

waveguide. Light reflected from the waveguide is directed by the 2 x 2 coupler to an optical spectrum analyzer.

The first step of the alignment process involves replacing the EDFA with a Helium Neon laser and imaging the transmitted near-field beam appearing at the back facet of the waveguide with a CCD camera. The Helium Neon laser is used because its wavelength falls within the spectral bandwidth of the CCD camera. The optical fiber and waveguide are first aligned visually, and then a five degree of freedom mono-positioning stage is used to adjust the location and orientation of the waveguide, while viewing the near field image on a video monitor. This process is stopped when the near-field image intensity is maximized, and its shape symmetric and centrally located. The He-Ne laser is then replaced with an EDFA, and the gap between the optical fiber and waveguide is reduced while monitoring the reflected spectrum in the spectrum analyzer. Optimum positioning is achieved when the spectrum associated with the airgap Fabry-Perot interferometer formed between the optical fiber and waveguide facet is minimized. Index matching liquid is the applied to the back facet of the waveguide sensor to prevent a Fabry-Perot cavity from forming between the two waveguide facets.

5. GRATING CHARACTERIZATION

5.1. Effective Refractive Index Measurements

The exact center wavelength of the grating reflectivity will vary with the effective index of the guided mode, which itself depends on the waveguide dimensions. As part of the grating evaluation process, the effective indices of the slab waveguides were measured using the intermodal spacing in the optical spectra produced by a Fabry-Perot interferometer purposefully formed between the two facets of the waveguide. This effective index[27] is given by

$$n_{eff} = \lambda_0^2 / 2(2\delta\lambda_w) \tag{5}$$

where λ_0 is the peak emission wavelength, $\delta\lambda$ is intermodal spacing of the waveguide cavity and L_w is the length of the cavity. The intermodal spacing of the waveguide cavity is measured using the EDFA in the arrangement shown in Fig. 5. In this case, however, steps are taken to promote Fabry-Perot interference between the two waveguide facets. This involves keeping a ~1 μm gap between the optical fiber lead and front facet, and not using an index matching liquid on the back facet. The resulting optical spectrum is viewed using an Advantest, Model Q8347 optical spectrum analyzer. This particular OSA enables the intermode spacing measurements 0.007 nm wavelength resolution.

Several waveguide sensors were fabricated using the techniques described in Section 3. Table 1 provides the measured and calculated values of the effective index of the waveguide at room temperature for four of these waveguides. The measured values are determined using Eq. (5) and the calculated values are determined using the results of Eq. (1). Note that these calculations were performed with n_1=1.0, n_2=1.4495, n_3=1.4452, t_g=8.0 μm, and λ_0=1550 nm. Table 1 also shows the waveguide length (distance between facets), the measured intermodal spacing, the Bragg wavelength calculated using Eq. (3), as well as the measured Bragg wavelength. This data shows that the measured effective indices and Bragg wavelengths of the slab waveguide

Table 1. Summary of the values of the effective refractive indices measured for the waveguides

Sensor	Waveguide Length L_w (mm)	Intermode Spacing $\delta\lambda_0$ (nm)	Measured Effective Refractive Index n_{eff}	Predicted Effective Refractive Index n_{eff}	Predicted Bragg Wavelength λ_b (nm)	Measured Bragg Wavelength λ_b (nm)
1	4.78	0.174	1.4452	1.4464	1555.79	1552.57
2	4.79	0.173	1.4495	1.4464	1555.79	1556.55
3	3.19	0.260	1.4483	1.4464	1555.79	1552.65
4	4.81	0.172	1.4481	1.4464	1555.79	1552.44

predicted values agree to within 0.21 %. This difference is most likely attributable to the measurement errors imposed by the spectrum analyzer resolution and variability in the waveguide thickness. Nevertheless, the data in Table 1 shows that the models developed in Section2 are sufficient for the purposes of waveguide sensor design and analysis.

5.2. The Reflectivity of the Grating

Fig. 6 shows the reflected spectrum produced by a grating 2 mm long, 200 nm deep (typical values) etched into a planar waveguide.

The reflected spectrum of the reflection from the planar waveguide gratings generally appeared bifurcated due to geometry-induced birefringence. Therefore, an output fiber polarizer is used to isolate the Bragg condition from one polarization mode. Typical values for the grating bandwidth and reflectivity are 0.2 nm and ~7 %, respectively. The reflectivity of this grating calculated with Eq. (4) and L=2.0 mm and a=200 nm is 7.1 %, which agrees with experiments to within 1.4 %, as shown in Fig. 7.

Also noticeable in the spectrum provided in Fig. 6 is small magnitude periodic artifact which is due to the Fabry-Perot cavity formed between the front and back facets of the waveguide. Although this effect was minimized by applying index matching fluid (refractive index, 1.4587) to be back facet of the planar waveguide, a small amount of light still resonated in the cavity due to imperfect index matching. Angle polish

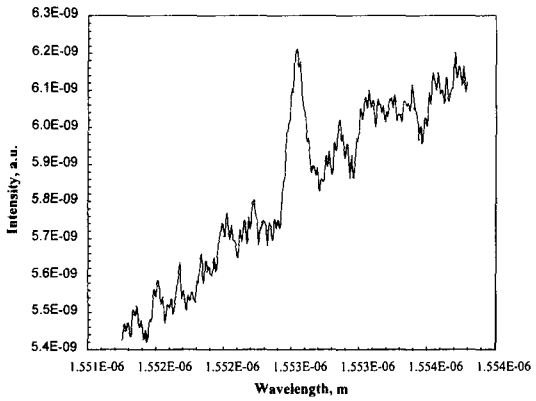

Fig. 6. Reflectivity of the etched planar waveguide Bragg grating sensor

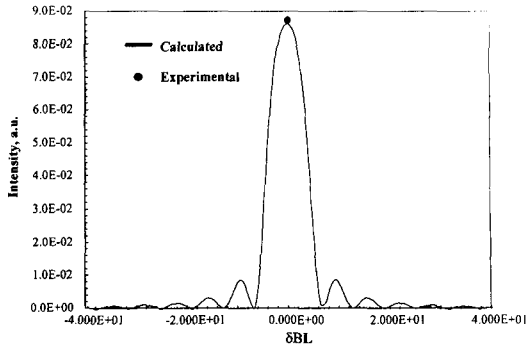

Fig. 7. Comparison of theoretical with measured in reflection spectrum of etched Bragg grating formed on the planar waveguide

ing the back facet of the waveguide is planned for future research to reduce Fabry-Perot effects to a larger degree.

5.3. Temperature Sensing

In order to examine temperature-sensing performance of the etched planar waveguide Bragg grating sensor, the planar waveguide Bragg grating was heated with temperature ranging from 20 °C to 200 °C using the heating tape. The resulting spectral shifts in the Bragg wavelength are monitored using the optical spectrum analyzer. A change in the temperature of the planar waveguide causes a shift in the Bragg wavelength due to thermal expansion, and the thermo-optic change in the effective index. The temperature-induced fractional wavelength shift[28] is given by

$$\Delta\lambda_b/\lambda_b = p_e\varepsilon + \zeta\Delta T \tag{6}$$

where ε is the thermal strain in the core of the waveguide, P_e=.79 is the strain-optic coefficient for silica, and ζ is the thermo-optic coefficient of the germanium-doped silica core[29]. This functional form for the temperature dependence of the core and cladding refractive indices are used with Eqs. (1) through (3) to calculate the temperature dependent effective thermo-optic response of the waveguide.

The slab waveguide is composed of two layers of materials with different Young's modulii and coefficients of thermal expansion. As a result, a change in temperature can cause a combination of expression of

expansion and warping. The degree of warpage will depend on the mismatch in thermomechanical properties and difference in thicknesses. This type of mechanical system can be analyzed using Classical Laminated Plate Theory (CLPT) often utilized in the analysis of laminated composites structures[30]. The incarnation of the CLPT used here is based on the following basic assumptions, (1) the layers within a laminate are considered perfectly bonded, (2) each layer is homogeneous, (3) each layer experiences plane stress conditions only, (4) plane sections remain plane. Following the CLPT approach, the strains on the surface of the waveguide is given by

$$\{\varepsilon\} = \{\bar{\varepsilon}^0\} + z\{\bar{k}\} \quad (7)$$

where $\{\bar{\varepsilon}^0\}$ is the global mid-plane strain, $\{\bar{k}\}$ is the global curvature, and z is the distance from the laminate mid-plane to the plane on which the strain is to be calculated. The CLPT can provide details of how the mid-plane strains and curvatures are derived in terms of the Young's modulii, coefficients of thermal expansion and thicknesses of SiO_2 waveguide and the silicon substrates. This analysis assumes that both the silica and silicon has isotropic mechanical properties (Table 2 provides the relevant properties[31,32]). Even though silicon is known to be anisotropic, the isotropy assumption is sufficient for the present analysis.

The material properties in Table 2 are used with Eq. (7) to calculate the thermal strain in the core of the waveguide. This strain is the substituted into Eq. (6) to estimate the thermally induced change in the Bragg wavelength. These calculating lead to a proportionality factor of 0.0122 nm/°C between the change in wavelength and temperature, as shown in Fig. 8.

The solid line in this figure is the wavelength response

Table 2. Materials properties of the silica and silicon

Materials	Thermal Expansion Coefficient, α(/°C) x 10^{-6}	Thermo-Optic Coefficient, ζ(/°C) x 10^{-6}	Young's Modulus, E (GPa)	Poisson's Ratio, ν
Silica	0.55	8.3	73	0.19
Silicon	2.63	--	190	0.27

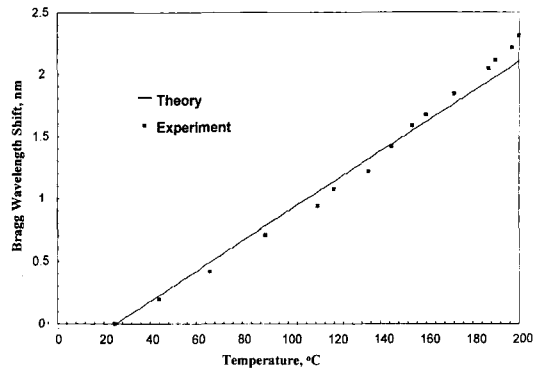

Fig. 8. Shifts in Bragg wavelength induced by temperature changes in etched planar waveguide sensor

predicted using Eq. (7). Typically, the temperature-induced fractional Bragg wavelength shift measured in this experiment varied linearly and is 0.0132 nm/°C, which is 7.5 % difference than the predicted slope. However, it is hard to compare the measured with the theoretical because the measured results show slightly nonlinear slope. For comparison, the proportionality factor for a ~1550 nm photorefractive grating written in an optical fiber is 0.0132 nm/°C. Fig. 9 shows the reflectivity at the Bragg wavelength as a function of temperature.

As seen in this figure, the reflectivity increases at temperature, 44°C. Up to about 100°C, the reflectivity is decreased. However, the reflectivity remain stable from 100°C. The origins of this effect are not clear, but a silica overcladding would likely reduce the variability. The spectral bandwidth of the grating was

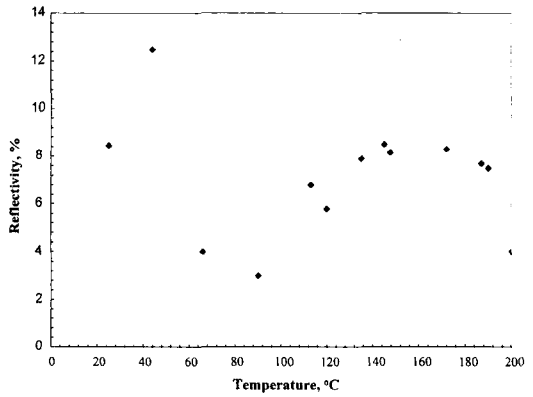

Fig. 9. Variation of reflectivity of Bragg wavelength in etched planar waveguide grating sensor with temperature changes

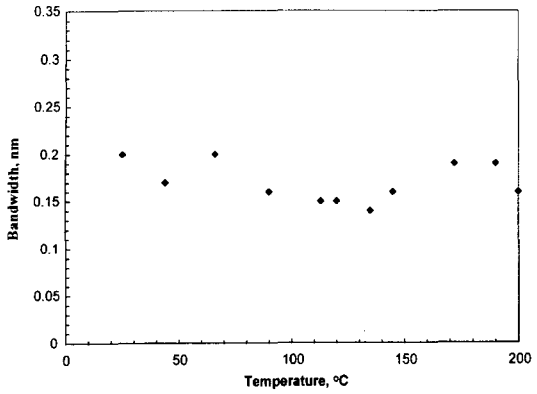

Fig. 10. Variation of bandwidth of Bragg wavelength in etched planar waveguide grating sensor with temperature changes

also measured as a function of temperature, as shown in Fig. 10, with no significant variations observed.

6. SUMMARY

An Optical temperature sensor based on the etched planar waveguide Bragg grating was developed and its performance was explored using theoretical and experimental methods. The planar waveguide is designed and fabricated using optical lithography and wet chemical etching. An efficient butt coupled optical fiber was used to examine the spectral characteristics of the grating sensor, and to investigate the grating parameters. Classical laminated plate theory with linear thermo-optic coefficient was combined in a simple model for the grating temperature response to predict the response of the temperature sensor. These theoretical predictions agreed to within 7.5% of the experimental measurements. This paper has demonstrated only the first step in developing high temperature strain gages and temperature sensors. Much work is still needed in device design and fabrication. This should include transition from planar to channel waveguides to minimize insertion loss. Methods of angle polishing the waveguide facets and for adding an amorphous silica overcladding should also be incorporated into the sensor fabrication. Only then will tests at extreme temperatures be possible. Even so, the results in this paper provide the fabrication and analysis frame work needed for continued development. Further work will be able to extend to reflect nonlinear temperature dependence of waveguide to theoretical analysis.

REFERENCES

1) T. Wu, L.-C. Ma and L.-B. Zhao, Exp. Mech. 21, 117, 1981.
2) L. D. Hudson, Proc. 6th Annual Conference On Hostile Environments and High Temperature Measurements, Society for Exp. Mech., 68, 1989.
3) W. A. Stange, AIAA/SAE/ASME 19th Jet Propulsion Conference., Seattle, WA, AIAA -83-1296, 1983.
4) J. F. Lei, H. Okimura and J. O. Brittain, Mat. Sci. Engi. A111, 145, 1989.
5) R. Harting, ISA 75251, 289, 1975.
6) B. E. Noltingk, Exp. Mech 15, 420, 1974.
7) E. B. Norris and L. M. Yeakley, ISA Nat'l Tech. Inform. Serv., PB 257, 1976.
8) C. C. Chang, D. Sagrario, L. Job and J. S. Sirkis. Proc. SPIE 2191, 482, 1994.
9) C. E. Lee and H. F. Taylor, IEEE J. Lightwave Tech. 9, 129, 1991.
10) R. R. Dils, J. Appl. Phys. 84 1198, 1983.
11) A. Wang, G. Z. Wang, S. Gollapudi, R. G. May, K. A. Murphy and R. O. Claus, Proc. SPIE 1798. 56, 1992.
12) T. E. Tsai, E. J. Friebele and D. L. Griscom, Opt. Lett. 18, 935, 1993.
13) T. Ergogan, V. Mizrahi, P. J. Lamaire and D. Monroe, J. Appl. Phys. 76, 73, 1994.
14) P. Miay, P. Bernage, M. Douay, T. Taunay, W. X. Sie, G. Martinelli, H. F. Bayon, H. Poignant and E.Devevaque, Proc. Photosensitivity and Quadratic Nonlinearity in Glass Waveguides: Fundamentals and Applications, OSA Technical Digest 22, 66. 1995.
15) C. V. Poulsen, Proc. Photosensitivity and Quadratic Nonlinearity in Glass Waveguides: Fundamentals and Applications, OSA Technical Digest 22, 100. 1995.
16) J. L. Archambault, L. Reekie and P. St. J. Russel. Electron. Lett. 29, 453, 1993.
17) T. Suhara and H. Nishihara, IEEE J. Quantum Electron 22, 845, 1986.
18) D. C. Flanders, H. Kogelnik, R. V. Schmidt and C. V. Shank, J. Appl. Phys. Lett. 24, 194, 1974.
19) R. V. Schmidt, D. C. Flanders, C. V. Shank and R. D. Standley, J. Appl. Phys. Lett. 25, 651, 1974.

20) C. S. Hong, J. B. Shellan, A. C. Livanos, A. Yariv and A. Katzir, J. Appl. Phys. Lett. 31, 276, 1974.
21) H. J. Lee, C. H. Henry, R. F. Kazarinov and K. J. Orlowsky, Appl. Opt. 26, 2618, 1987.
22) A. Yariv, IEEE J. Quantum Electron 9, 919, 1973.
23) Tatsuo Izawa, Hidefumi More, Yasuji Murakami and Nobuo Shimizu, J. Appl. Phys. Lett. 38, 483, 1981.
24) K. O. Hill, Y. Fugii, D. C. Johnson and B. S. Kawasaki, J. Appl. Phys. Lett. 32, 647, 1978.
25) W. W. Morey, G. Meltz and W.H. Glenn, Opt. Lett. 14, 823, 1989.
26) W. M. Moreau, Semiconductor Lithography: Principles, Practices, and Materials, New York: Plenum Press, 646, 1988.
27) J. J. Veselka and S. K. Korothy, IEEE J. Quantum Electron 22, 930, 1986.
28) W. W. Morey, G. Meltz and W. H. Glenn, Proc. SPIE 1169, 98, 1989.
29) S. Takahashi and S. Shibata, J. Non-Crystall. Solids 30, 359, 1979.
30) R. M. Jones, Mechanics of Composites Materials, New York:McGraw-Hill, 1975.
31) K. E. Petersen, Proc. IEEE 70, 420, 1982.
32) A. Kelly, Strong Solids (2nd ed. Oxford England: Clarendon, 1973.